Engineering Failure Analysis 192 (2026) 110863

Contents lists available at ScienceDirect

Engineering Failure Analysis

journal homepage: www.elsevier.com/locate/engfailanal

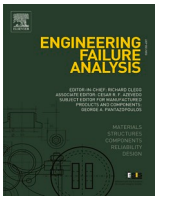

Thermal degradation and failure analysis of common-rail injectors in a dual-fuel marine engine: A combined numerical and experimental study

Seyfi Polat [a,b,*], Xiaoguo Storm [a], Martin Axelsson [c], Jari Hyvönen [c], Maciej Mikulski [a]

[a] Efficient Powerterain Solutions (EPS), School of Technology and Innovation, University of Vaasa, Wolffintie 34, FI-65200 Vaasa, Finland
[b] Faculty of Aeronautics and Astronautics, Department of Aviation Management, Adana Alparslan Türkeş Science and Technology University, 01250, Adana, Türkiye
[c] Engine Research and Technology Development at Wärtsilä Marine Solutions, FI-65101 Vaasa, Finland

ARTICLE INFO

Keywords:
Injector failure
Common-rail
Dual-fuel
Marine engine
Ansys

ABSTRACT

This study investigates the failure mechanisms of common-rail fuel injectors used in state- of-the-art dual-fuel marine engines. Combining numerical simulations and experimental tests, the research analyses the operational dynamics of the injector used in the diesel-mode cylinders that provide the required boost pressure for the dedicated reactivity-controlled compression ignition (RCCI) cylinder. A 3D computational fluid dynamics (CFD) model was developed to evaluate temperature and fuel velocity fields within the injector, while engine tests identified critical failure modes linked to abnormal fuel injection behaviour. Key findings reveal that a fuel supply limitation in the engińes speed control idle mode triggers uncontrolled speed drops when loads exceed 267 kW, leading to secondary injection peaks and prolonged high-temperature exposure. Thermal simulations highlight significant non-uniform temperature distributions, with the injector's bottom region reaching 435 °C during high duration operation, doubling low-state values. This elevated temperature propagates to the injectoŕs solenoid coil and causing insulation degradation. The study concludes that sustained high temperature, exacerbated by boundary condition shifts, is a primary driver of coil insulation failure. These insights emphasise the need for enhanced thermal management strategies and adaptive control algorithms to mitigate injector failures in marine and high-efficiency engines.

1. Introduction

Precise control of fuel injection is essential for achieving high efficiency and low emissions in modern internal combustion engines, particularly those using advanced combustion strategies like reactivity-controlled compression ignition (RCCI). Fuel injection directly influences ignition, combustion behaviour and overall engine performance. Optimal performance of engine requires a clear understanding of the injector's operation, such as the timing of fuel injection, the amount of fuel delivered and the spray pattern [1]. Any

* Corresponding author at: Efficient Powerterain Solutions (EPS), School of Technology and Innovation, University of Vaasa, Wolffintie 34, FI-65200 Vaasa, Finland.
E-mail address: seyfi.polat@uwasa.fi (S. Polat).

https://doi.org/10.1016/j.engfailanal.2026.110863
Received 24 September 2025; Received in revised form 11 March 2026; Accepted 7 April 2026
Available online 8 April 2026
1350-6307/

inaccuracies in these can lead to uneven fuel mixing, improper ignition timing or incomplete combustion, all of which can significantly affect the engine's efficiency and emissions [2]. Real-time monitoring and control of fuel injection are necessary to make the most of engine's potential, adapting to changes in engine operating conditions and fuel properties. This ensures that combustion remains stable and efficient, while also minimising undesirable outcomes such as knock or high levels of particulate matter. Therefore, achieving fine-tuned control over the injector's performance is key to fully exploiting the benefits of engine and pushing the limits of current internal combustion engine technologies.

The cost of maintaining a vessel's engine is high, but the costs associated with unplanned maintenance and repairs can be far greater due to the lost revenue from the vessel being out of service [3]. Accurate injector state estimation has helped in predicting failures before they occur, allowing for more efficient scheduling of maintenance activities. Identification of early signs of injector issues has allowed operators to avoid expensive repairs and unplanned downtime, ensuring vessels remained operational and profitable. A reliable system for injector state estimation is a critical component in managing the operational costs and efficiency of marine engines, ultimately contributing to the reduction of both direct and indirect costs in marine operations.

Injector faults could severely impact engine performance, leading to impaired fuel efficiency and greater emissions. These issues could also result in engine misfire or damage, leading to costly repairs. Ke et al. [4] presented an early fault diagnosis method for common rail injectors, combining cyclostationary blind deconvolution (CYCBD) optimised by the Seagull optimisation algorithm (SOA) and hierarchical fluctuation dispersion entropy (HFDE). It filtered fuel pressure signals using CYCBD and extracted fault characteristics with HFDE, overcoming the limitations of traditional entropy methods. The fault features were classified using least squares support vector machines (LSSVM). Experimental results showed that this method outperformed existing approaches in fault recognition accuracy. Gallego et al. [5] explored the failure of API J55 steel tubings due to localised corrosion in water injector wells at an oil field. The degradation mechanisms were determined through microscopy, chemical analysis and computational fluid dynamic (CFD) simulations. They revealed that sulphate-reducing bacteria (SRB) were responsible for pitting corrosion and cracking. The results showed that corrosion rates were particularly high under calcareous deposits in watertight areas with flow rates less than 0.17 m/s. The study suggested that while fluid stagnation could not be avoided, cathodic protection with sacrificial electrodes was the most effective method to prevent SRB-induced corrosion in the tubing. Taghizadeh et al. [6] investigated fault detection of injectors in diesel engines through vibration time–frequency analysis. The authors employed techniques such as Welch test, short-term Fourier transform (STFT), Wigner-Ville distribution (WVD) and Choi-Williams distribution (CWD) to examine vibrations generated by an engine. The results indicated that faulty injectors produced vibrations in the 10–25 kHz frequency range, which affected engine performance. The STFT technique proved to be the most efficient for fault diagnosis and knock detection in real-time performance monitoring. Additionally, the RMS and kurtosis values of faulty injectors increased by 12.9% and 20.6%, respectively. Song [7] presented a high-precision fault diagnosis method for high-pressure common rail injectors by combining improved fruit fly optimisation algorithm (IFOA) with variational mode decomposition (VMD) and hierarchical dispersion entropy (HDE). The proposed method aimed to address the challenges of adaptive signal decomposition and fault diagnosis accuracy. Using engineering test data, the method demonstrated better computational efficiency and classification accuracy than other methods. Jan Monieta [8] introduced a method using vibration and in-cylinder pressure signals to diagnose cracks in injector nozzles of marine internal combustion engines. The research highlighted the use of advanced signal processing techniques, including decimation, wavelet analysis and machine learning to detect damage development during real-time operations of vessels. The study demonstrated that new diagnostic symptoms, identified through these methods, were more effective than traditional ones in detecting damage.

Thermal analysis was not yet widely applied in fault diagnostics, despite its potential to provide valuable insights into the condition of the injector and its armature. Li et al. [9] presented a numerical analysis of an internally-cooled strut injector for scramjet engines, utilising a coiled and miniature cooling configuration to enhance thermal management. The proposed design significantly reduced coolant mass flow requirements while achieving high heat transfer efficiency. The study highlighted the impact of non-uniform pressure distribution in the manifold on mass flow deviations and pressure drop, providing insights into optimising cooling strategies for extreme aerodynamic hesating conditions. Chakravarty et al. [10] investigated the impact of side injection on heat removal in a truncated conical heat-generating porous bed, using a thermal non-equilibrium approach. Their study demonstrated that cold fluid injection enhanced convective heat transfer, with porous media permeability significantly influencing flow dynamics. The findings provided insights into optimising cooling strategies for heat-generating porous materials in various thermal management applications. Liu et al. [11] conducted a thermal analysis of a 170 GHz gyrotron's magnetron injection gun (MIG) using Ansys Workbench and Comsol Multiphysics. The results showed that the cathode emission band experienced a temperature difference of 4.6 ℃, with a total deformation of approximately 0.054 mm, which was within an acceptable range and had minimal impact on MIG performance. The simulation results from both software platforms were consistent, demonstrating the effectiveness of thermal analysis in assessing electron gun performance at high temperatures.

As mentioned above, most studies of injector faults have concentrated on issues like nozzle clogging, coking and corrosion, which directly impacted engine performance, fuel efficiency and emissions. These faults were typically diagnosed by analysing vibrations, fuel pressure signals and corrosion patterns using advanced techniques such as time–frequency analysis, signal decomposition and entropy measures [4–14]. However, little attention was paid to the influence of temperature fields on injector failure, particularly in terms of the degradation of the coil insulation layer. This current study introduces a novel approach by using a 3D nozzle model and employing computational fluid dynamics (CFD) tools to analyse the overall temperature field within the injector. This provides new insights into how temperature variations affect the performance and longevity of high-pressure common rail injectors, extending the focus of fault diagnosis beyond traditional issues related to nozzles and corrosion.

2. Methods

2.1. Common-rail fuel injector

Fig. 1 depicts the image of the solenoid common-rail injector. This injector is employed in some variants of medium-speed diesel engines for marine and power generation applications. Designed for high injection precision and durability under varying load conditions, the injector supports flexible fuel delivery strategies enabled by the common-rail system. Detailed specifications of the injector are defined according to engine configuration and manufacturer standards.

The structure of the common-rail injector can be divided into solenoid system (mainly consisting of solenoid, solenoid spring, armature part); passage system (mainly consisting of fuel inlet, fuel return, valve control valve and control chamber) and needle-nozzle assembly (mainly consisting of needle, needle chamber and nozzle) [16]. The solenoid system provides electromagnetic force to overcome resistance of the solenoid spring when there is current loaded on solenoid, controlling the lifting and seating of the needle by moving valve. Fuel goes into control chamber through the fuel inlet. When the electromagnetic force from the solenoid is high enough, the valve control plunger will be pulled up, so fuel will enter the needle system. Extra fuel will flow back to common rail system after injection through the fuel return. The needle-nozzle assembly is responsible for shaping the fuel mass-flow profile and spray atomisation. Table 1 lists the injectoŕs main parameters.

The working process of the common rail injector can be outlined in four stages. During the closing stage (i) there is no excitation current on the solenoid coil, so the armature is kept far from the seat by pre-leaded spring force and hydraulic resistance. The bleed orifice is also closed and the fuel flow into the control chamber is prohibited.

The opening stage (ii) starts when the driving current is loaded on the solenoid coil. The electromagnetic force ramps up and, after overcoming resistance, the armature moves downward. The bleed orifice opens up and fuel flows from control chamber back to common rail thorough fuel return. This causes a drop in hydraulic force exerted on the valve control plunger, while the pressure in needle chamber equalises with the rail pressure. Eventually, the hydraulic force lifts the needle and fuel injection commences. The excitation current should be large enough in the solenoid coil to allow the needle to lift up as soon as possible to achieve the required SOI (start of injection).

During the holding stage (iii), the armature is seated and the air gap between the coil and plunger becomes very small. The electromagnetic force is inversely proportional to air gap, so it is not necessary to provide high current to keep the needle lifted. Decreasing the electrical load is necessary from the perspective of mitigating the heat generated in the solenoid coil. The holding stage lasts until injection duration ends.

The closing stage (iv) commences when the injection duration ends. The driving current will be cut, and without electromagnetic force, the armature will rapidly move upwards, closing the bleed valve. The fuel supply to the needle chamber will be shut off, and injection will stop. One should note that during armature movement, the armature will collide with the seat and rebound continuously, causing mechanical vibration.

Fig. 1. Image of the common-rail injector [15].

Table 1
Specification of the solenoid common rail injector.

Description	Value
Injector type	common rail
Type of actuation	solenoid control
Spray type	C (conical spray)
Hole number	9
Hole diameter [mm]	0.3
Cone angle [degree]	153
Operating pressure [bar]	600 to 2200
Voltage level [V]	110
Pick current [A]	6
Hold current [A]	4
Coil resistance [Ohm]	3

2.2. Engine test setup

The engine used in this test is a research grade version of a state-of-the-art Wärtsilä 20 medium speed engine. The test cell is located at the University of Vaasa's Energy Laboratories. The research version of the engine has a four-cylinder in-line configuration, with single-stage turbocharger. Each of the 200 mm-bore cylinders has a 200 kW per cylinder nominal power output. The engine has been modified for this test to operate in a prototype dual-fuel RCCI mode, with one cylinder running with natural gas and diesel, while the other three cylinders run in standard diesel mode with the factory-installed, ultra-high pressure common-rail direct-injection (CRDI). The RCCI-enabled cylinder is positioned furthest from the flywheel, as shown in Fig. 2. In this work, the injector under investigation is taken from one of the diesel-mode cylinders, which are essential for providing the boost pressure that stabilizes the combustion process in the RCCI cylinder and thereby enables reliable dual-fuel operation.

The entire engine is loaded by a 1050 kW alternating current (AC) squirrel-cage generator, which is connected to the grid through a frequency converter. Table 2 lists key data of the engine and the test bed.

The common-rail injector system operates by maintaining a constant high-pressure fuel supply in a shared rail which delivers fuel to the injectors. Fig. 3 depicts a schematic diagram of the system. This arrangement decouples fuel injection from engine speed, allowing for more precise control of fuel delivery. The engine control unit (ECU) manages the timing and quantity of fuel injected into each cylinder, optimising combustion efficiency. This independent control enables the injectors to function at a constant pressure, regardless of changes in engine speed, resulting in improved performance, reduced emissions and better fuel efficiency [17,18].

The independent operation of the pilot common-rail system, through separate control and separate fuel delivery, allows for enhanced flexibility and precision in engine management. Unlike the stock common-rail system, where all injectors draw fuel from a shared high-pressure rail and are controlled simultaneously or sequentially by a centralised strategy, the separate system employs individually managed actuators and fuel paths for each injector. This structural and functional separation enables independent tuning of injection parameters per cylinder, improving control accuracy.

By decoupling fuel injection from engine speed, both systems provide better atomisation and more efficient combustion, but the separate system adds further refinement by allowing fully customised injection timing and quantity on a per-cylinder basis. The ECU adjusts the timing and volume of fuel injected into each cylinder, regardless of load or speed, improving the engine's response across various operating conditions.

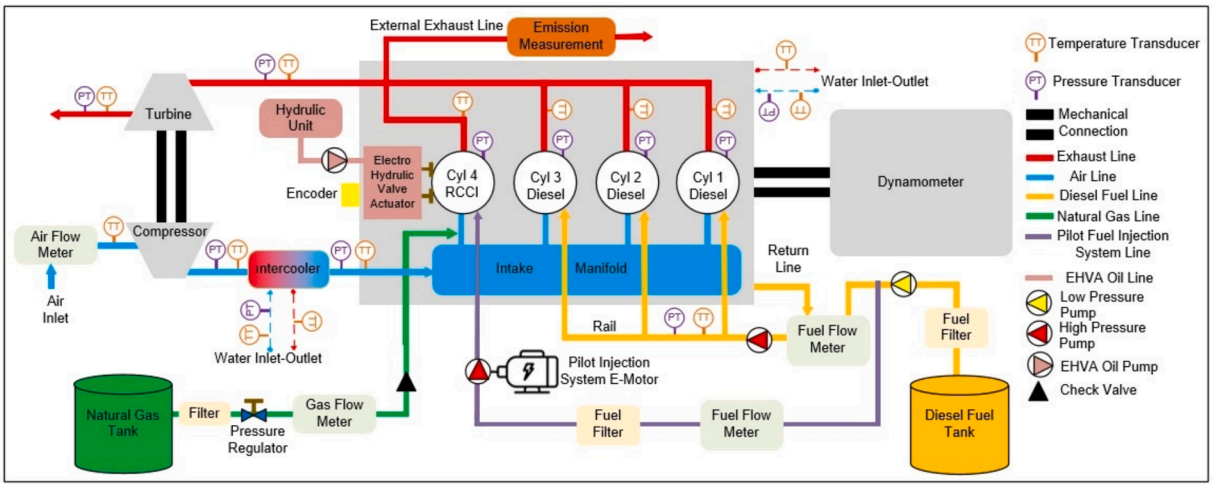

Fig. 2. RCCI cylinder and related subsystems.

Table 2
Specification of the Wartsila 4 L20 research engine with RCCI retrofit.

Engine	Wärtsilä 4 L20 Diesel	RCCI retrofit
Cylinder configuration	four-cylinder, inline	semi-decoupled one-cylinder with common air path and individual fuel paths
Bore [mm]/ stroke [mm]	200 / 280	200 / 280
Cylinder displacement [dm^3]	8.8	8.8
Compression ratio	15.8	13.44
Diesel fuel system	CRDI – Wärtsilä, engine-driven HP pump; solenoid common rail injector	CRDI – Independent electrically-driven HP pump; solenoid common rail injector
Gas fuel system	–	PFI 20 bar
Valve system	Cam-based four valves/cylinder	EHVA four valves/cylinder
Airpath	Single stage turbocharger; up to 8 bar boost pressure, charge air cooler	
Rated RPM	1000	

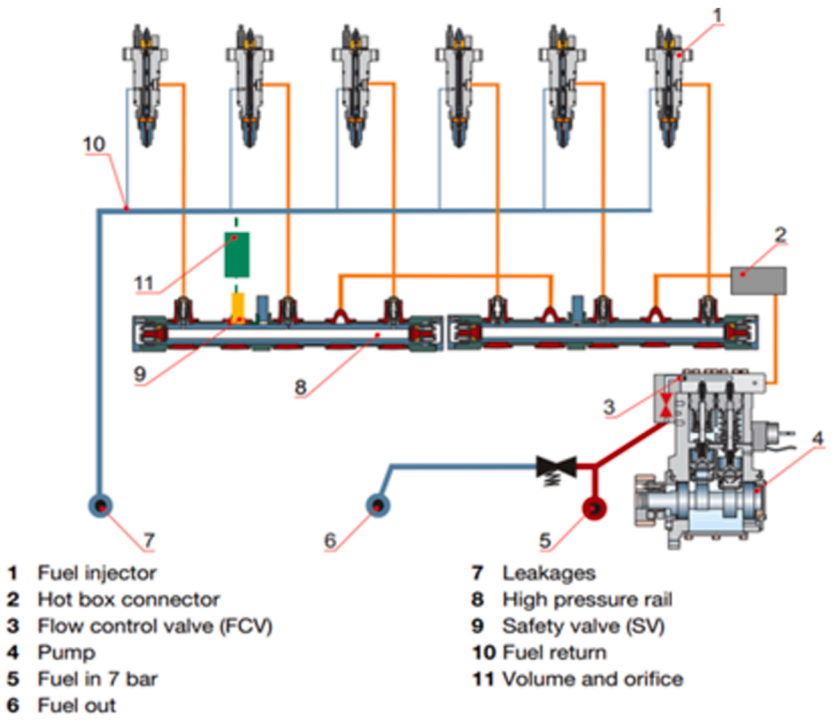

Fig. 3. Structure of the common-rail system [15].

Target machine serves as the ECU in this test bench, as shown in Fig. 4. The target machine real-time target machine is used to implement the injector control unit and other control units on this platform. It supports a wide variety of industrial input–output connectivity protocols, such as those for speed, load and temperature signals. This system is designed for rapid prototyping in research applications, primarily for regulating engine parameters to maintain the engine speed at a given reference point.

The target machine sends monitoring signals specific to the engine and electrical system to the central data acquisition system via a Modbus interface. Engine signals that change slowly, such as temperatures, pressures, fuel consumption and emissions, are sampled every second. High-frequency sampling, triggered by an optical encoder, is used for more dynamic signals, such as in-cylinder pressure and injection currents. This allows synchronisation with the engine's rotational angle, with a resolution of 0.1 crank angle (CA) degrees. Additionally, relays are used to capture signals related to the electrical system.

2.3. Simulation models

2.3.1. Mathematical model of control system

Fig. 5 is a schematic diagram of the speed control system. The speed feedback unit sends the speed detected by the speed sensor into the speed controller. Based on the speed deviation, the speed controller performs a series of calculations according to the designed control strategy, feeding control instructions to the actuator to adjust the amount of fuel supplied to the diesel engine [19].

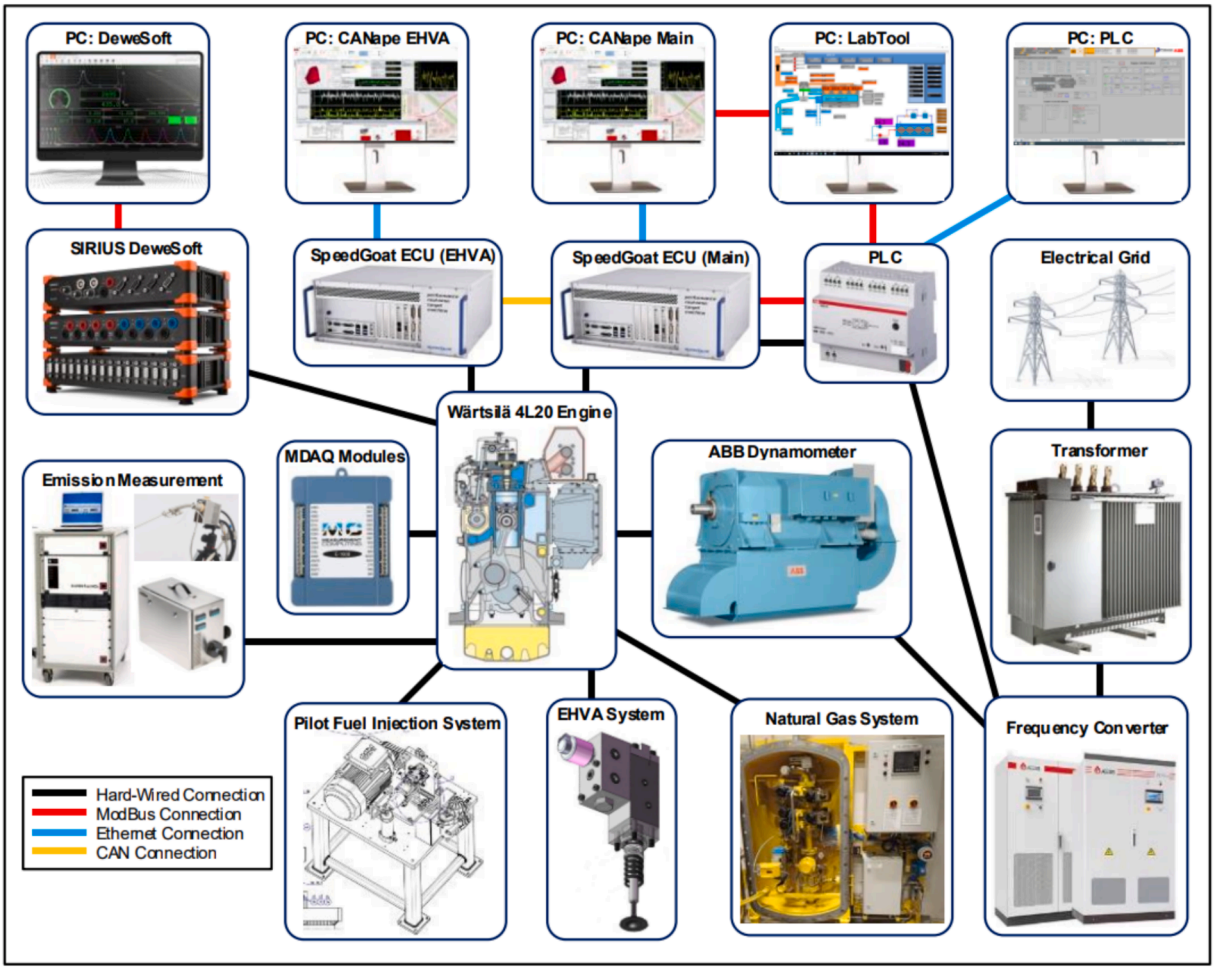

Fig. 4. Schematic view of electronic management of the engine test setup.

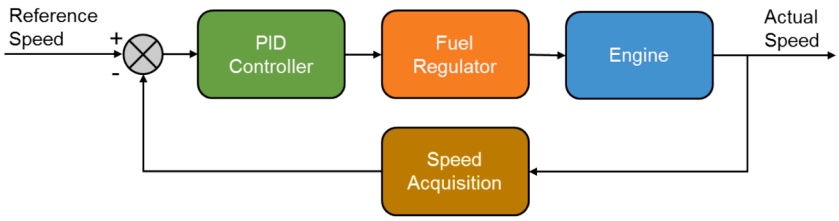

Fig. 5. Flow diagram of the speed control system.

The proportional-integral-derivative (PID) controller compares the feedback speed with the set speed to calculate the control signal deviation of PID parameters according to pre-calibrated speed and load map, ensuring robust controller performance under changing operating conditions. Based on this control logic, the development of a dynamic model becomes essential for capturing the engine's transient behaviour under varying loads. To this end, D'Alembert's principle is introduced as a foundational tool for transforming the dynamic equations of motion into an equivalent static form. By treating inertial forces as reversed external forces, this principle allows us to analyse the system in terms of force balance, simplifying the derivation of control-relevant models. It forms the basis for understanding how the system responds to sudden load changes, and ultimately supports the design of a control algorithm that ensures speed stability during such transients.

According to D'Alembert's principle, the equation of motion for the diesel engine can be written as Equation (1):

$$j\frac{dw}{dt} = M_d - M_c \tag{1}$$

where j is the moment of inertia transferred to the crankshaft from the diesel engine; M_d is diesel engine output torque; and M_c is resistive torque.

Considering that the output torque M_d is related to the fuel injection quantity g and engine angular velocity w, one can expand the term around the equilibrium point M_do using the Taylor series. Neglecting the quadratic and higher-order terms, one obtains Equation (2) for the output torque:

$$M_d + \Delta M_d = M_d o + \left(\frac{\delta M_d}{\delta w}\right)\Delta w + \left(\frac{\delta M_d}{\delta g}\right)\Delta g \tag{2}$$

The resistive torque Mc similarly can be expanded as partial derivative of the angular velocity ω and the engine load L.

Including both assumptions in Equation (1), and assuming the engine is at equilibrium state ($Md_o = Mc_o$), one obtains Equation (3):

$$j\frac{d\Delta w}{dt} + F \cdot \Delta w = \left(\frac{\delta M_d}{\delta g}\right)\Delta g - \left(\frac{\delta M_c}{\delta L}\right)\Delta L \tag{3}$$

where the term F denotes the difference between partial derivatives of Mc and Md over w, respectively. In that sense, the diesel engine's self-stability coefficient is used to measure the stability of the engine operating conditions.

The relation between w, g and L can be defined using the dimensionless formula in Equation (4):

$$\frac{\Delta w}{w_e} = \phi, \frac{\Delta g}{g_e} = \eta, \frac{\Delta L}{L_e} = \lambda \tag{4}$$

where w_e is nominal engine rpm. The terms g_e and L_e denote respectively the fuel consumption and engine load at nominal engine rpm.

Considering the above Equation (3) can be re-written as the set of equations, Equation (5):

$$T_a\frac{d\phi}{dt} + T_g\phi = K_\eta\eta - K_l\lambda \tag{5}$$

$$T_a = \frac{Jw_e}{M_d e} \tag{5.a}$$

$$T_g = \frac{Fw_e}{M_d e} \tag{5.b}$$

$$K_\eta = \frac{\left(\frac{\delta M_d}{\delta g}\right)}{\left(\frac{M_d e}{g_e}\right)} \tag{5.c}$$

$$K_l = \frac{\left(\frac{\delta M_c}{\delta L}\right)}{\left(\frac{M_d e}{L_e}\right)} \tag{5.d}$$

T_a is referred to as the diesel engine acceleration time constant. Its physical significance is the time required for the engine's angular velocity to reach the rated angular velocity, starting from zero under no-load conditions. It should be noted that the control-related coefficients appearing in the above mathematical formulation are implemented within a commercially calibrated, map-based engine management framework; therefore, they are not fixed scalar constants but operating-point-dependent parameters obtained through prior experimental optimization and embedded in the proprietary engine management system.

From a control perspective, one very important characteristic of the diesel engine is that ignition occurs in a specified sequence over a small number of cylinders, resulting in intermittent power generation. This characteristic is important for two main reasons.

First, it indicates that there is a delay before the engine responds to the action of the governor and the change in fuel consumption rate. This delay has always been an unstable factor in control systems. Second, the engine crankshaft does not rotate at a constant speed, but is frequently subjected to periodic torque variations, leading to periodic speed fluctuations. This instability must be eliminated by the governor's drive mechanism, taking into account ignition delay. Equation (6) is yielded as:

$$T_a\frac{d\varphi}{dt} + T_g\varphi = K_\eta(t-\tau) - K_l\lambda \tag{6}$$

After applying the Laplace transform to the above equation, the transfer function of the diesel engine, Equation (7), can be obtained as:

$$\frac{\Phi(S)}{K_\eta e^{-\tau s}H(S) - K_l\Lambda(S)} = \frac{1}{T_a s + T_g} \tag{7}$$

The control system assumes the load is supplied by the motor, and load fluctuations are neglected. By approximating the delay term

as $e^{\tau s\ c} \approx 1 + \tau s$, the system can be represented by Equation (8):

$$\frac{\Phi(S)}{H(S)} = \frac{1}{(T_a s + 1)(1 + \tau s)} \tag{8}$$

2.3.2. CFD and mechanical model

A 3D model of an injector seat was set up by the Ansys software. The injector seat is embedded in the cylinder head, in direct contact with the mixture gas in the cylinder, so the injector seaťs thermal condition reflects the general thermal condition of cylinder. Due to commercial confidentiality restrictions, permission to reproduce the exact proprietary injector geometry was not granted; consequently, a geometrically representative approximation was constructed for the numerical simulations. The injector has four orifices, each with a diameter of 0.8 mm. The model is partitioned into a mechanical part, which accounts for the structural characteristics of the injector seat, and a fluid part, which represents the internal flow dynamics.

To account for turbulence effects in the fluid domain, the Transition SST ($\gamma - Re_{\theta t}$) turbulence model was employed to describe the internal diesel flow within the injector. This model is formulated on the basis of the k–ω SST framework and incorporates additional transport equations for intermittency (γ) and the transition momentum thickness Reynolds number ($Re_{\theta t}$), allowing the prediction of laminar-to-turbulent transition within boundary layers. Considering the high injection velocities, strong pressure gradients, and complex internal nozzle geometry, accurate representation of near-wall flow behaviour and transition effects is required. The Transition SST ($\gamma - Re_{\theta t}$) model enables the resolution of boundary layer development and transition phenomena under such conditions, providing improved prediction of velocity, pressure, and temperature fields in high-pressure internal injector flows [20,21].

In the present study, a low-y^+ wall treatment approach was adopted to accurately resolve near-wall flow behaviour. The computational mesh was refined in the boundary layer region to ensure that the dimensionless wall distance y^+ remained close to unity. This approach enables direct resolution of the viscous sublayer without relying on wall-function approximations. Given the high-pressure gradients and strong shear effects inside the injector, accurate prediction of near-wall velocity gradients and heat transfer is critical. The low-y^+ formulation therefore improves the fidelity of wall shear stress, thermal flux, and transition modelling, particularly when coupled with the Transition SST ($\gamma - Re_{\theta t}$) turbulence model. This ensures more reliable representation of boundary layer development under high-speed internal flow conditions.

To accurately represent the high-pressure fuel flow within the injector, the fluid was treated as compressible, allowing its density to vary with pressure and temperature. Given the operating pressures exceeding 120 MPa, density variations cannot be neglected. Although steady-state operating conditions were assumed for the simulations, the governing equations were formulated under a compressible flow framework to capture pressure-dependent thermophysical behaviour. Under these assumptions the conservation of mass equation can be described as:

$$\frac{\delta\rho}{\delta t} + \frac{\delta(\rho u)}{\delta x} + \frac{\delta(\rho v)}{\delta y} + \frac{\delta(\rho w)}{\delta z} = 0 \tag{9}$$

where ρ represents the density of the fluid; u, v, and w are the components of the velocity vector in the x, y, and z directions; and t is the time, measured in seconds.

In the flow field, the rate of increase of energy within a fluid element is equal to the net heat flux entering the fluid element plus the work done by body forces or surface forces on the fluid element. Under these assumptions the energy conversation equation can be described as:

$$\frac{\delta(\rho T)}{\delta t} + div(\rho u T) = div\left(\frac{k}{c_p}\mathrm{grad}T\right) + S_T \tag{10}$$

where c_p and T represent the specific heat capacity and thermodynamic temperature of the fluid, respectively; k is the thermal conductivity of the fluid; and S_T represents the internal heat source of the fluid and the portion of mechanical energy within the fluid that is converted into thermal energy.

Fuel flows from the low-pressure system into the high-pressure pump, where it is compressed in the plunger chamber by the plunger. This results in increased pressure and a rise in oil temperature within the outlet passage. When fuel is continuously delivered to the common rail, it flows through pipelines of varying cross-sections within the rail, causing the outlet temperature to vary depending on the common-rail pressure. As the fuel is delivered to the injector and flows through the small-diameter orifices, the

Table 3
Boundary condition of fluid area.

Boundary	Parameter	Low Duration State	Steady Duration State	High Duration State
Inlet	Pressure (MPa)	130	140	120
	Temperature (°C)	105	110	95
Outlet	Velocity (m/s)	$\frac{\partial v}{\partial n} = 0$		
	Mass flow rate (kg/s)	0.042	0.0437	0.0402
Wall	Pressure (MPa)	$\frac{\partial p}{\partial n} = 0$		
	Velocity (m/s)	v = 0		

throttling effect causes a temperature rise in the fuel. As the common- rail pressure and injection pulse width increase, the throttling-induced heat generation of the fuel inside the injector becomes more significant, leading to a rising trend in the fuel temperature at the injector outlet [22]. When the common-rail pressure reaches 140 MPa, the injector inlet temperature is set to 110 ℃; when common rail pressure is 120 and 130 MPa, the injector inlet temperature is set to 95 ℃ and 105 ℃ respectively. These pressure–temperature values correspond to experimentally measured average fuel temperatures obtained under the respective operating conditions. Table 3 lists the boundary conditions of the fluid area.

The grid size in the CFD mesh is set to 5 mm. However, since the fluid flow in the injector operates under turbulent conditions, it is crucial to include a boundary layer near the walls, especially in areas where the flow transitions from laminar to turbulent. This allows for a more accurate representation of the velocity and thermal boundary conditions at the solid–fluid interface. Grid refinement to enhance simulation accuracy is applied to smaller dimensional areas, such as the nozzle holes, where high gradients of velocity, pressure and temperature are expected. Fig. 6 depicts the mesh optimisation. These areas are critical for the accurate prediction of the spray dynamics and heat transfer within the injector. This grid refinement allows the simulation to capture the fine details of flow behaviour which would otherwise be averaged out in a coarser grid, leading to potential inaccuracies.

The flow field of diesel determines the temperature boundary and heat transfer coefficient in the internal region of the injector. Therefore, the numerical simulation results of the fluid domain will be applied to the injector's overall temperature field, providing boundary conditions for its calculation.

Turning to the mechanical model, the injector seat consists of a needle chamber and nozzle, as shown in Fig. 1. The fuel pressure acts on the needle valve, creating an upward motion tendency, while the regulating spring force on the upper part of the needle valve resists this upward motion, preventing the needle valve from moving upwards. When fuel pressure $<$ spring force, the needle valve does not move, and the sealing cone of the needle valve is tightly pressed against the valve seat, preventing fuel from being injected. When fuel pressure $>$ spring force, the upward force from fuel pressure overcomes the spring force, causing the needle valve to move upwards. This lifts the sealing cone away from the valve seat, allowing the needle valve chamber to communicate with the pressure chamber. High-pressure fuel then flows from the pressure chamber through the injector holes and is injected into the engine combustion chamber. When the needle valve reaches its maximum lift, its upward movement is halted by the mechanical stop provided by the injector limit block. Considering that injector faults occur during active operation with the injector nozzles fully open, the modelling approach disregards the needle and its effects on the flow and temperature fields.

The nozzle tip is exposed to the intensely hot combustion chamber, directly in contact with the high-temperature gas during engine operation. Its thermal state is similar to that of the cylinder wall, especially the fire side of the cylinder head. When the diesel engine operates under stable conditions, the components in the combustion chamber experience frequent temperature fluctuations due to the impact of combustion gases. However, these fluctuations only occur in a very thin layer at the surface of the heated parts, with small amplitude, and the fluctuation amplitude decays exponentially [23]. Therefore, it can be considered that the thermal load on the fuel injector is steady and constant.

The thermal boundary condition can be divided into three parts, shown in Fig. 7. Q1 area is the external surface of injector, which has direct contact with cylinder gas by way of heat transfer. Q2 area is embedded into the cylinder cover, so the heat transfer condition is the same as the cylinder cover. Q3 area is the internal surface of the injector seat and nozzle, where the heat transfer condition is forced heat convection.

The outer surface of the injector nozzle tip (Q1) is continuously subjected to direct heat transfer from high-temperature gases throughout the engine's operating cycle. The presence of intake and exhaust valves allows for brief convective heat exchange between the cylinder and the external environment, leading to variations in the heat transfer coefficient of the fluid medium along the inner surface of the cylinder wall at the same axial height. However, these differences are negligible due to the minimal flow area within the

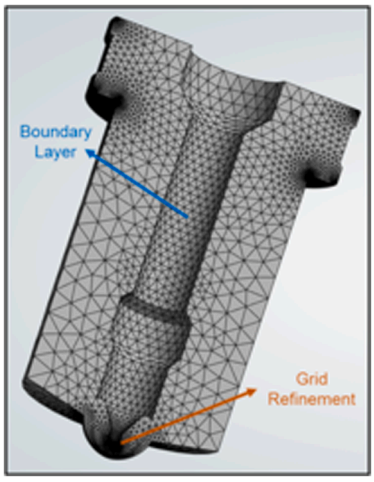

Fig. 6. Meshing optimisation.

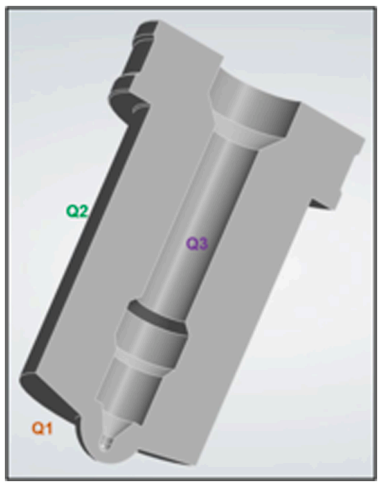

Fig. 7. Different thermal boundary areas of the injector seat.

cylinder. Therefore, it can be assumed that the heat transfer coefficient is uniform along the inner surface of the cylinder wall at the same axial height [24,25]. Consequently, the boundary conditions for the temperature field analysis in Q1 area can be determined as follows:

$$\begin{cases} \alpha_e = \dfrac{1}{\tau_0}\displaystyle\int_0^{\tau} \alpha d\tau \\ T_c = \displaystyle\int_0^{\tau_0} \alpha T d\tau \Big/ \int_0^{\tau_0} \alpha d\tau \end{cases} \tag{11}$$

where α_e and T_c represent the average heat transfer coefficient and the comprehensive average temperature of the engine gas over one working cycle, respectively; αis the instantaneous heat transfer coefficient of the gas; and T is the instantaneous temperature of the gas.

The heat transfer coefficient can be expressed as:

$$\alpha = 3.26 B^{-0.2} p^{0.8} T^{0.55} w^{0.8} \tag{12}$$

where B is the diameter of piston in m; p is average gas pressure in kPa; T is gas temperature in Kelvin; and w is the average gas velocity in m/s.

Since the Q1 region is located directly within the combustion chamber, its surface is in direct contact with the in-cylinder gases throughout the engine cycle. Consequently, both the gas temperature and the associated convective heat transfer coefficient vary instantaneously depending on the combustion phase and operating condition. To determine the local ambient temperature and heat transfer coefficient in the Q1 region, cycle-based calculations were performed for each operating condition as low duration, steady duration and high duration states. These parameters were obtained using the experimental data together with the empirical correlation given in Eq. (12), enabling the in-cylinder gas temperature and corresponding heat transfer coefficients to be determined on a cycle-averaged basis for each specific working condition. Table 4 lists the boundary condition parameters of low duration, steady duration and high duration states.

Q2 area is embedded within the cylinder head, so its thermal boundary conditions are presumed to correspond to those of the cylinder head. The cylinder head temperature stabilises around 185–225 °C depending on the engine load condition, with a corresponding heat transfer coefficient of 80 W/m2·K. Heat transfer in the Q3 region is predominantly influenced by the internal flow behaviour of the fuel within the injector. The thermal boundary conditions are determined through a coupling analysis conducted in Ansys, where the temperature distribution extracted from the fluid domain is accurately applied to the injector's inner surface to capture the interaction between fluid flow and structural heat transfer.

The temperature distribution within the injector directly influences the thermal behaviour of the solenoid coil. Consequently, the results of the numerical simulation of the injector temperature field serve as thermal boundary conditions for predicting the

Table 4
Boundary condition of Q1 area of three states.

State	Temperature (℃)	Heat transfer coefficient (W/m^2 K)
Low duration	576	651
Steady duration	645	938
High duration	864	1456

temperature rise in the coil.

2.3.3. Modelling of injector coil

Two factors affect the rise in coil temperature: heat flow coming from electrical current and heat transfer with environmental temperature.

Considering heat flow caused by electrical current, the coiĺs resistance is impacted by temperature. The resistance of coil can be defined by Equation (13):

$$R(T) = R_0 \cdot [1 + \alpha \cdot (T - T_0)] \tag{13}$$

where R_0 is initial resistance; α is coefficient of material, for bronze α is 0.0039 k-1; T is temperature in coil; and T_0 is initial temperature.

The heat power transmitted through the coil can be expressed as follows:

$$P = I^2 R \tag{14}$$

where I is electric current; and R is defined according to Equation (13).

For heat transfer with environmental temperature, the heat flow of convectional heat transfer between coil and environment can be expressed as follows:

$$Q = h \cdot A \cdot (T_c\text{-}T_a) \tag{15}$$

where h is convectional coefficient; A is contact area between coil and fuel; T_c is coil surface temperature; and T_a is air temperature.

The section of the injector located above the injector seat is thermally insulated from the combustion gases, so it maintains a stable thermal condition. Accordingly, the ambient temperature surrounding the solenoid coil is assumed to be equivalent to the temperature at the upper surface of the injector seat, as derived from the fluid–structure coupled numerical model. Table 5 lists the boundary conditions employed for the thermal analysis of the coil. As depicted in Fig. 8, the coil is modelled with a wire diameter of 2 mm, a coil height of 40 mm and an overall coil diameter of 16 mm.

2.3.4. Mesh independency and residual values

To ensure mesh independence, a series of simulations were conducted using progressively refined cell counts for each model configuration, and an optimization was performed to balance computational cost with numerical accuracy. Table 6. presents the results of the mesh independence analysis performed for the injector mechanical model, the coupled injector fluid + mechanical model, and the coil mechanical model. The temperature and velocity variations obtained at different mesh densities are evaluated relative to the reference solution in order to quantify the influence of mesh refinement on numerical accuracy and solution convergence. The mesh sensitivity study was systematically conducted up to Test 5 for each model configuration. As the number of elements increases from Test 1 to Test 5, a consistent and substantial reduction in solution deviations is observed. In the coupled injector fluid + mechanical model, the mesh density reaches 1,032,522 elements in Test 5, where the temperature variation decreases to 0.20 K (0.03%) and the velocity variation reduces to 0.54 m/s (0.0009%). These values indicate that the solution has effectively reached a mesh-independent regime, as the incremental changes between successive refinements become negligibly small.

Similarly, in the injector mechanical model, the finest mesh configuration (Test 5, 73,054 elements) yields a temperature variation of only 0.01 K (0.08%), demonstrating strong numerical stability with respect to further refinement. For the coil mechanical model, Test 5 (24,531 elements) results in a temperature deviation of 0.35 K (0.21%), which likewise confirms convergence behaviour within an acceptable engineering tolerance.

Table 7 presents the final residual values obtained after convergence for the low, steady, and high duration operating states. A total of 2000 iterations were performed for each case, and all governing equations reached stable residual levels within the predefined convergence limits. The continuity residuals are on the order of 10^{-3}, while momentum equations (x, y, and z velocity components) converge to the order of 10^{-5}. The energy equation exhibits residuals between 10^{-5} and 10^{-4}, indicating strong thermal convergence. Similarly, the turbulence-related quantities, including turbulent kinetic energy (k), specific dissipation rate (ω), intermittency (γ), and transition momentum thickness Reynolds number ($Re_{\theta t}$), demonstrate consistent convergence behaviour with residual levels between 10^{-5} and 10^{-4} across all operating states. These results confirm the numerical stability and reliability of the solution procedure for the different injection duration conditions.

Table 5
Boundary condition of the injector coil.

State	Current (A)	Voltage (V)	Duration (ms)	Environmental temperature (°C)	Heat transfer coefficient (W/m2 K)	Temperature coefficient of resistance
Low duration	6	110	3.0	Derived from fluid-mechanical model	30	0.0065
Steady duration			3.6			
High duration			5.7			

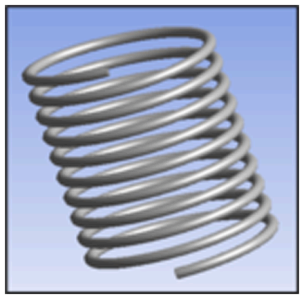

Fig. 8. 3D model of the injector coil.

Table 6
Mesh independence of injector and coil.

Part and Module	Parameters	Test 1	Test 2	Test 3	Test 4	Test 5
Injector Mechanical	Number of Elements	2178	6719	10,353	23,940	**73,054**
	Variation of Temp. (K)	Ref.	0.66	0.13	0.02	0.01
	Variation of Temp. (%)	0	2.89	0.57	0.09	0.08
Injector Fluid + Mechanical	Number of Elements	142,262	328,866	884,105	944,217	**1,032,522**
	Variation of Temp. (K)	Ref.	6.8	3.95	0.35	0.2
	Variation of Temp. (%)	0	1.07	0.62	0.05	0.03
	Variation of Velocity (m/s)	Ref.	12.8	5.3	0.5	0.54
	Variation of Velocity (%)	0	0.02	0.009	0.0008	0.0009
Coil Mechanical	Number of Elements	9324	6732	8974	14,102	**24,531**
	Variation of Temp. (K)	Ref.	2.64	0.7	1.06	0.35
	Variation of Temp. (%)	0	1.6	0.42	0.65	0.21

Table 7
Final Residual Values for Different Operating States.

Parameter	Low Duration State	Steady Duration State	High Duration State
Continuity	1.00×10^{-3}	1.00×10^{-3}	1.00×10^{-3}
x-velocity	4.00×10^{-5}	4.00×10^{-5}	4.00×10^{-5}
y-velocity	2.00×10^{-5}	3.00×10^{-5}	3.00×10^{-5}
z-velocity	3.00×10^{-5}	3.00×10^{-5}	3.00×10^{-5}
Energy	4.00×10^{-5}	5.00×10^{-5}	7.00×10^{-5}
Turbulent kinetic energy (k)	4.00×10^{-4}	5.00×10^{-4}	5.00×10^{-4}
Specific dissipation rate (ω)	3.00×10^{-4}	3.00×10^{-4}	3.00×10^{-4}
Intermittency (γ)	2.00×10^{-5}	2.00×10^{-5}	2.00×10^{-5}
Transition momentum thickness Reynolds number ($Re_{\theta t}$)	5.00×10^{-4}	5.00×10^{-4}	5.00×10^{-4}

Maciej Mikulski reports financial support was provided by Bussines Finland. Xiaoguo Storm reports financial support was provided by Bussines Finland. Seyfi Polat reports financial support was provided by Bussines Finland. Seyfi Polat reports financial support was provided by TUBITAK. If there are other authors, they declare that they have no known competing financial interests or personal relationships that could have appeared to influence the work reported in this paper.

3. Results and discussion

The results section is structured to gradually enhance the understanding of injector performance, focusing on different aspects of its operation. It begins with an analysis of the engińes behaviour under varying load conditions, providing insight into the systeḿs overall dynamics. Thermal and fluid flow analyses follow, helping to assess the impact of temperature variations and fluid movement on injector performance. The section then shifts to a detailed investigation of the coil's behaviour, particularly focusing on its failure mechanisms. Each of these analyses builds upon the previous one, progressively contributing to the development of a comprehensive diagnostic framework for injector failure.

3.1. Results of injection failure observed during the engine tests

Fig. 9 presents significant parameters related to engine speed control observed during the experiments. The engine performance can be categorised into three distinct phases, based on the control of the injection duration: the low duration state (prior to load increase), the steady duration state and the high duration state.

Step 1. Closed-loop control:

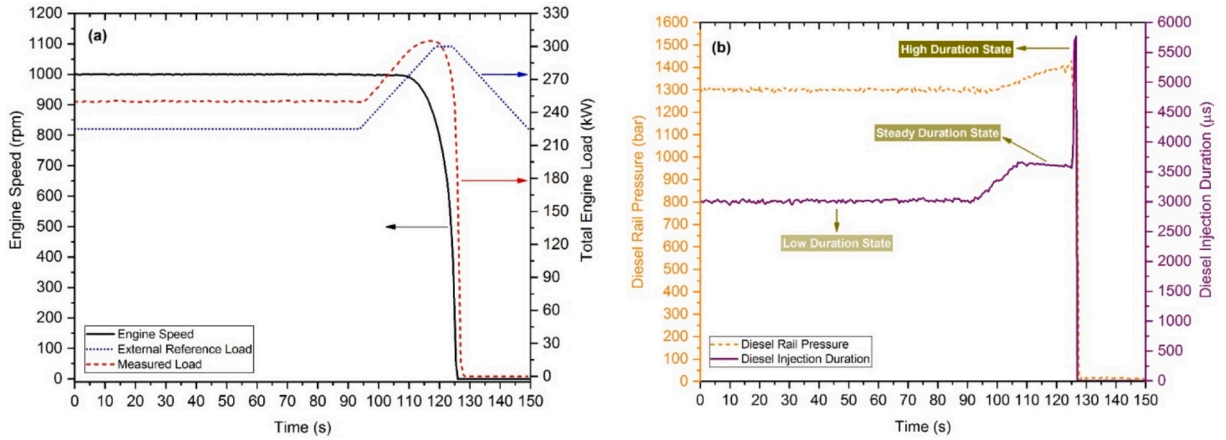

Fig. 9. Variation of engine load, diesel injection pressure and duration during speed control.

Initially, as the external load increases from 220 kW, both engine speed and torque remain constant. During this period, injection duration and diesel injection pressure gradually increase, indicating that the control system maintains closed-loop regulation. The stable response of all monitored parameters suggests effective control action within this phase.

Step 2. Speed drop:

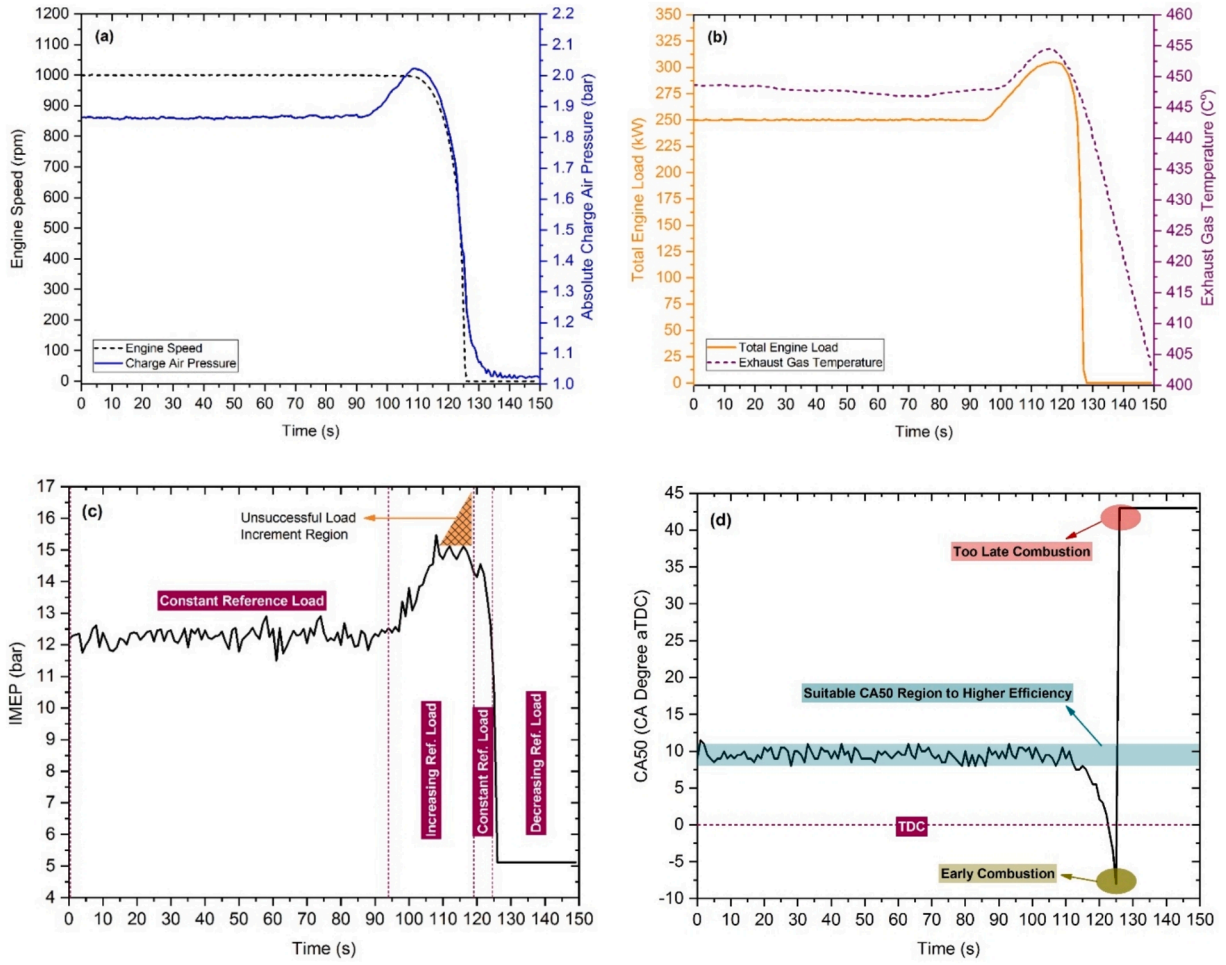

Fig. 10. Thermal behaviour as engine speed drops.

Upon reaching an external load of approximately 267 kW, the engine speed begins to deviate from its set point, indicating a loss of closed-loop control. The engine speed drops, despite a steady injection duration and fuel demand. Given that the injection duration is directly proportional to the fuel supply, maintaining closed-loop control of the engine speed under increasing load conditions necessitates a corresponding rise in fuel delivery. The observed decline in engine speed implies that fuel supply is insufficient to meet the increasing load demand. Nevertheless, the engine torque continues to rise, while other parameters exhibit abnormal behaviour, further indicating instability.

Step 3. High duration:

As the engine speed decreases to critically low levels, a sudden and significant increase in injection duration is observed, rising sharply from 3000 μs to 5700 μs. Concurrently, other operational parameters begin to deteriorate. Since fuel demand is directly proportional to injection duration, this abrupt rise leads to an increased fuel demand. Subsequently, injector failure is observed. The strong correlation between the rapid escalation in injection duration and the occurrence of injector failure suggests a causal relationship. This issue will be explored in greater detail in the subsequent section.

Fig. 10 shows the thermal behaviour of the engine during the speed reduction phase. In the low-duration state, the test engines operation is stable at a constant speed of 1000 rpm under a load of 220 kW, with a charge air pressure of 1.85 bar, an exhaust gas temperature of approximately 450 °C, an IMEP of around 12 bar and a CA50 occurring at 10 degrees after top dead center (aTDC), which is favourable for achieving high thermal efficiency. When the engine reference load is increased to 267 kW, in what is defined as the steady-duration state, the engine speed remains stable at 1000 rpm up to a certain load. Due to the increased fuel injection into the cylinder with rising load, the total released heat energy also increases, and IMEP rises from 12 bar to approximately 15 bar. Additionally, the increased heat release inside the cylinder leads to a rise in exhaust gas temperature and, consequently, an increase in charge air pressure. However, before reaching the target reference load of 267 kW, the engine speed begins to decline, and IMEP starts to decrease without reaching the expected level. Simultaneously, the increasing gap between the reference load and the measured load necessitates greater fuel injection, leading to an extension of the injection duration. The rapid decrease in exhaust gas flow rate as the engine speed drops causes a sharp decline in charge air pressure, reducing the amount of intake air. Since the fuel injection quantity remains unchanged during this phase, the cylinder mixture becomes progressively richer. This shift leads to a change in CA50, from approximately 10 degrees aTDC, towards around 8 degrees before top dead center (bTDC), meaning the combustion phasing advances toward the compression stroke. Essentially, the entire combustion is advanced, and the shift of combustion into the compression phase causes an increased negative IMEP region, and thus a reduction in the net IMEP value. Although the reference load is subsequently reduced back to 220 kW, extremely high injection durations are reached during the high-duration state, indicating a significant deviation from stable operating conditions.

3.2. *Pre-investigation of the fault cause using a reduced order model*

Two distinct control modes are implemented in the engine speed control framework: idle control mode, for regulating engine speed under no-load conditions; and speed control mode, for speed regulation under loaded operating conditions. Due to an erroneous configuration, the engine operates under the idle control mode even during load application. In the idle control mode, the PID controller limits for fuel demand are set to 4000 periods per ten-thousand (pptt) at high engine speeds and 6000 pptt at lower speeds. In

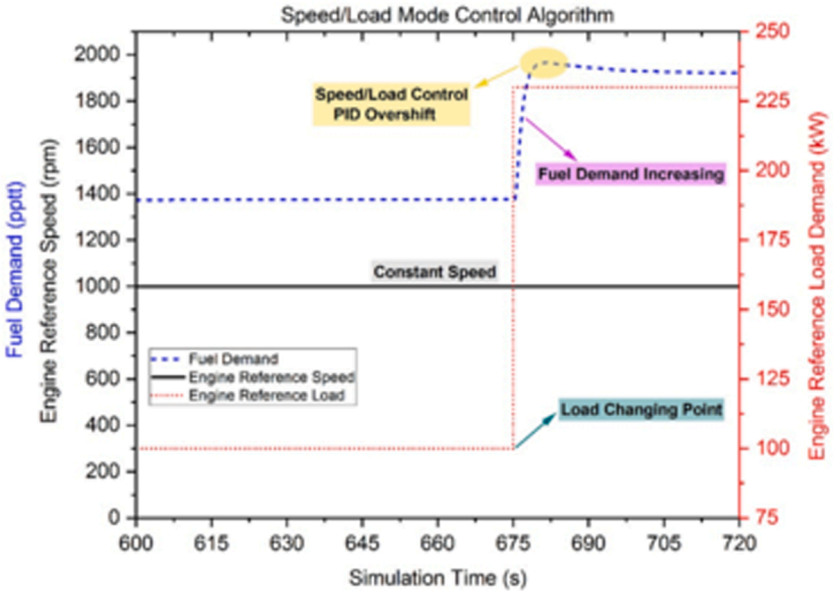

Fig. 11. Speed closed-loop control in speed control mode.

contrast, the corresponding limit for fuel demand in the speed control mode is configured at 10,000 pptt. This disparity implies that, at a speed reference of 1000 rpm, the maximum permissible output – corresponding to the fuel demand – is restricted to 4000 pptt in idle control mode. This settinġs insufficient fuel delivery capability hampers the engine's ability to maintain the desired speed under load, ultimately leading to deviations from stable operation. The relationship of engine load with torque and speed can be depicted as a mathematical model as:

$$P = \frac{T \cdot N}{9550} \tag{16}$$

where T is engine torque; and N is engine speed. Torque T can be also expressed in form of IMEP:

$$T = \frac{IMEP.V_s}{4\pi} \tag{17}$$

where V_s is engine displacement volume. So, Equation (18) can be yielded as:

$$P = \frac{IMEP.V_s.N}{4\pi \cdot 9550} \tag{18}$$

As the external load increases, the engine needs to generate a corresponding rise in torque to maintain operational stability. In response to load increments, a natural tendency for engine speed to decline is observed. The greater the external load, the more pronounced the decrease in engine speed. As IMEP is directly proportional to the fuel supply, maintaining a constant engine speed under varying load conditions necessitates a proportional increase in fuel demand. However, within the constraints of the idle control mode, the maximum allowable fuel demand is limited to 4000 pptt. This constraint establishes an effective load threshold beyond which the required fuel compensation exceeds the predefined limit. Consequently, the engine control system becomes incapable of maintaining speed stability once this load threshold is surpassed, resulting in a progressive drop in engine speed.

Fig. 11 presents the simulation results of the speed control mode, conducted within the MATLAB/Simulink environment. The engine maintains a stable speed under speed control mode, despite changes in the reference load. Even when there is a large discrepancy between the reference load demand and the actual load, the control system increases the engine load gradually due to ramp-up limitations, until the target load is reached. The control system actively compensates for changes in the reference load by dynamically adjusting the fuel demand, thereby ensuring that the engine consistently delivers the required power output without compromising speed stability. Specifically, with an increase in load, the fuel demand correspondingly rises to meet the additional energy requirements, allowing the engine speed to remain constant. This effective closed-loop regulation demonstrates the robustness of the speed control strategy in maintaining engine performance under varying load conditions.

Fig. 12 depicts the simulation results of the idle control mode, performed within the MATLAB/Simulink environment. The reference speed is set to 1000 rpm, while the reference load remains at zero to emulate no-load operating conditions. Initially, the fuel demand remains constant, even if an external load is applied or a load request is issued. Consequently, due to the unadjusted fuel supply, the engine speed begins to decline as load increases. Once a deviation from the reference speed is detected, the control system actively compensates by increasing the fuel demand, thereby restoring the engine speed to its nominal reference value. This control strategy maintains stability during idle operation while providing the necessary adaptability to accommodate variations in external load, ensuring consistent engine performance under transient conditions.

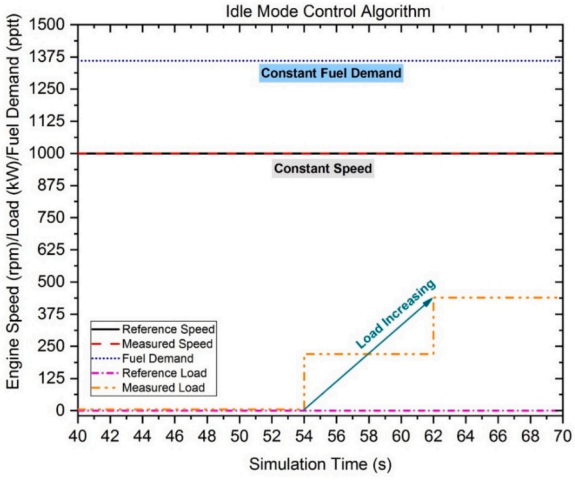

Fig. 12. Speed closed-loop control in idle control mode.

3.3. Results of CFD and mechanical analysis

Figs. 13 and 14 illustrate the velocity distribution of diesel fuel under three different states, inside the injector and within the nozzle. Except within the nozzle region, the fuel velocity remains relatively uniform throughout the injector body, with the maximum velocity reaching approximately 47 m/s. However, a significant increase in velocity is observed within the nozzle, indicating a higher heat transfer coefficient relative to other regions of the injector. The peak velocity inside the nozzle is observed slightly below the hole centre, corresponding to the red regions in the velocity contour map. This pattern is caused primarily by the guiding effect of the pressure chamber walls and the nozzle wall. As the flow approaches the nozzle wall, the fuel velocity gradually decreases due to viscous effects and the development of a velocity gradient near the wall.

In all states, the velocity in the nozzle reaches to 620 m/s, with peak velocities located in the vicinity of the nozzle exit region. Despite minor variations in velocity magnitudes among the different conditions, the overall velocity profile remains largely unchanged among the three states, indicating that variations in inlet and outlet boundary conditions have no substantial effect on injector flow behaviour. These results demonstrate stable flow characteristics under all examined state conditions, with no significant deviations observed in the velocity distribution profiles.

Fig. 15 illustrates the temperature distribution of diesel fuel within the injector under three different operating conditions. Immediately downstream of the fuel inlet, the temperature in the central core region largely preserves the imposed inlet temperature. However, as the flow approaches the injector's internal solid surfaces, the fuel temperature begins to increase due to heat transfer from the surrounding injector walls. Progressing further toward the nozzle tip region, the thermal influence becomes more pronounced. The elevated heat flux transmitted from the combustion chamber to the injector's mechanical components raises the inner wall temperature, which in turn enhances conductive and convective heat transfer to the adjacent fuel. As a result, the fuel temperature gradually increases along the axial direction toward the injector tip. The highest fuel temperatures are observed in regions located near the upper corner of the injector seat, where the thermal load originating from the combustion chamber is most significant. This distribution indicates that the internal fuel temperature field is predominantly governed by conjugate heat transfer between the heated injector structure and the flowing fuel, rather than by inlet boundary effects alone.

Figs. 16 and 17 illustrate the temperature fields and peak temperatures for all states. They show that the temperature field inside the injector exhibits non-uniform distribution, primarily influenced by the structural characteristics of the injector and spatial variations in boundary conditions. The highest temperature is observed in the bottom area of the injector (Q1), where the temperature gradient is also the most significant. This is primarily attributed to the direct contact between the injector wall and the in-cylinder gas mixture, which induces high heat transfer rate and leads to elevated local temperatures. Conversely, regions adjacent to the internal fuel flow path exhibit relatively lower temperatures. This occurs because the fuel temperature is considerably lower than the surrounding solid temperature, thereby reducing local thermal levels in these regions. In particular, the fluid area (Q3) exhibits a lower temperature than the solid area (Q1) because the temperature of the fluid is much lower than the surrounding environmental temperature. Additionally, the Q2 and Q3 areas are influenced by lower ambient temperatures, which, in combination with the convection heat transfer from the surrounding fluid, result in a more uniform temperature distribution. These regions show less temperature variation, indicating that the fuel flow conditions and the heat transfer contribute to the relatively uniform thermal behaviour observed.

Changes in the boundary conditions, particularly in the Q2 area, have a significant effect on the overall temperature distribution within the injector. In low duration state, external load remains unchanged, and the maximum temperature reaches 241.5 ℃. As the convection heat transfer coefficient and the ambient temperature increase, the maximum temperature in the high duration state reaches 435.2 ℃, which is approximately 44.8% higher than the maximum temperature observed in the steady duration state (300.4 ℃). This substantial increase in temperature is a direct result of the enhanced convection heat transfer, which allows more heat to be transferred from the surrounding environment into the injector. Furthermore, the boundary conditions in the Q2 area not only affect the temperature distribution in the Q2 region but also influence the temperature profiles in the adjacent Q1 and Q3 areas. The overall temperature in these areas in the high duration state is higher than in the other two states, demonstrating the significant impact of the modified boundary conditions. This increase in temperature underscores the importance of boundary conditions in determining the thermal performance and heat distribution within the injector, particularly in areas directly affected by changes in convection heat transfer and ambient conditions.

Fig. 18 shows that the temperature rise within the injector coil is predominantly influenced by the surrounding temperature, rather than by the electrical current itself. Although resistive heating contributes to the coil's temperature rise, the increase attributable to the electrical current is approximately 10 °C, relatively minor compared with the dominant influence of the ambient temperature. Variations in injection duration affect the duration of current flow but do not significantly alter the current's heat contribution, suggesting that the electrical input plays a secondary role in determining the coil's overall thermal behaviour.

In contrast, the ambient temperature exerts a considerably stronger thermal influence on the coil. Fig. 16 shows that the region above the injector seat remains thermally stable, so the temperature at the top surface of the injector seat is used as the effective ambient temperature for the coil. This ambient temperature varies with injection duration, directly affecting the heat transfer into the coil body. Specifically, the maximum coil temperature reaches 163 ℃ in the high duration state, compared to 128 ℃ and 114 ℃ in the steady and low-duration states, respectively. These results highlight the dominant role of ambient thermal conditions in determining the final temperature of the injector coil.

Fig. 18 shows that the temperature distribution along the coil exhibits a relatively uniform thermal profile with a consistent axial gradient. Nevertheless, minor local fluctuations are observed, potentially arising from material inhomogeneities, particularly variations in the temperature coefficient of resistance. These inconsistencies may lead to localised variations in heat generation, resulting in

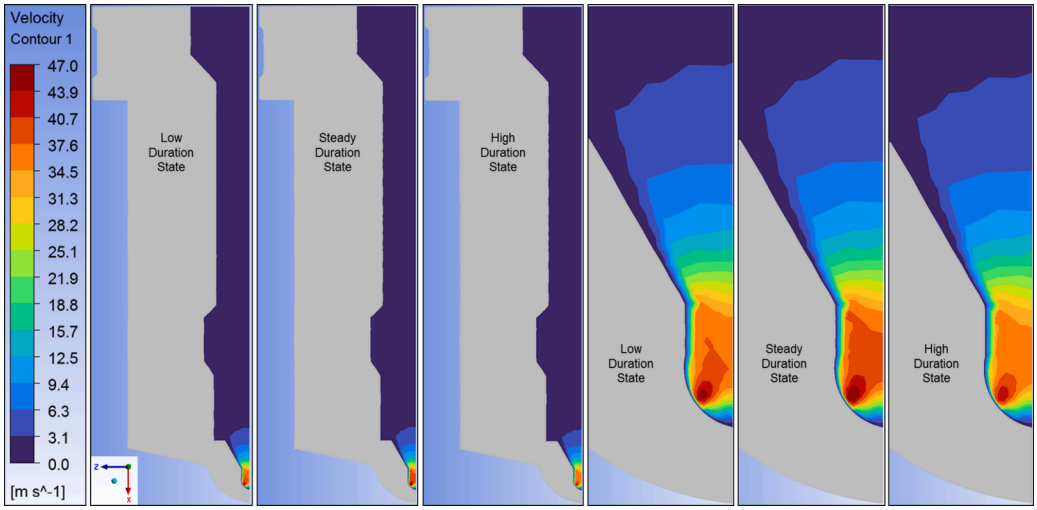

Fig. 13. The velocity distribution of the fuel along the central longitudinal section of the injector.

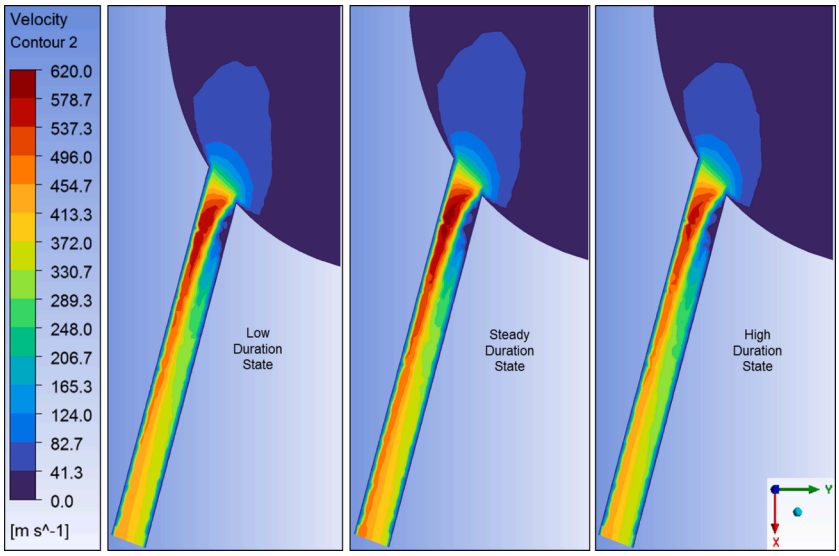

Fig. 14. The velocity distribution of fuel inside the injector nozzle.

slight deviations in the thermal field, even under otherwise steady-state conditions.

3.4. Evaluation of injector failure

Post-experiment inspections revealed no visible physical damage to the injector. However, a marked increase in coil resistance was observed, indicating potential degradation of the coil's insulation. Thermal stress is recognised as the primary cause of drive coil failure, with inter-turn insulation breakdown being the most prevalent failure mechanism. The coil temperature increased during high duration state, and these high thermal loads significantly affect the performance of the insulation layer within the solenoid coil windings. Coil materials are specifically designed to provide electrical isolation between adjacent turns, but the insulation begins to thermally degrade when temperatures exceed the material's designated operational threshold. This degradation disrupts the molecular structure, causing loss of mechanical flexibility and tensile strength. Consequently, the material becomes increasingly susceptible to micro-cracking and eventual structural failure. Moreover, repeated thermal cycling due to continuous expansion and contraction during temperature fluctuations, induces mechanical stress in the insulation, often resulting in micro-cracks or delamination. Excessive localised heating near the coil further accelerates insulation breakdown. High temperatures also facilitate moisture ingress into the insulation, especially under high-humidity environmental conditions. Moisture absorption reduces insulation resistance, thereby compromising its dielectric strength and increasing the risk of electrical leakage or short-circuiting. Overall, sustained high

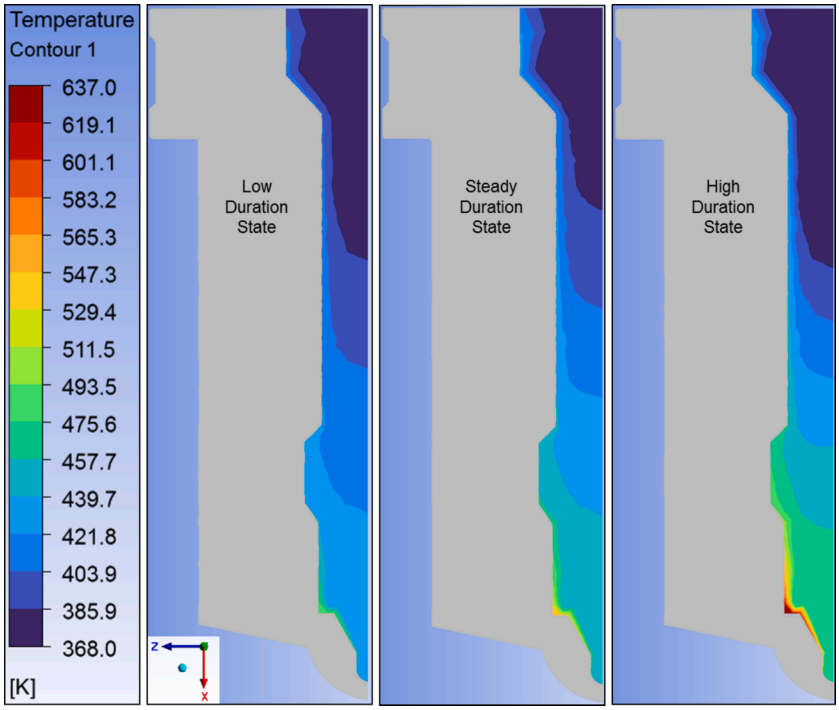

Fig. 15. The temperature distribution of fuel inside the injector.

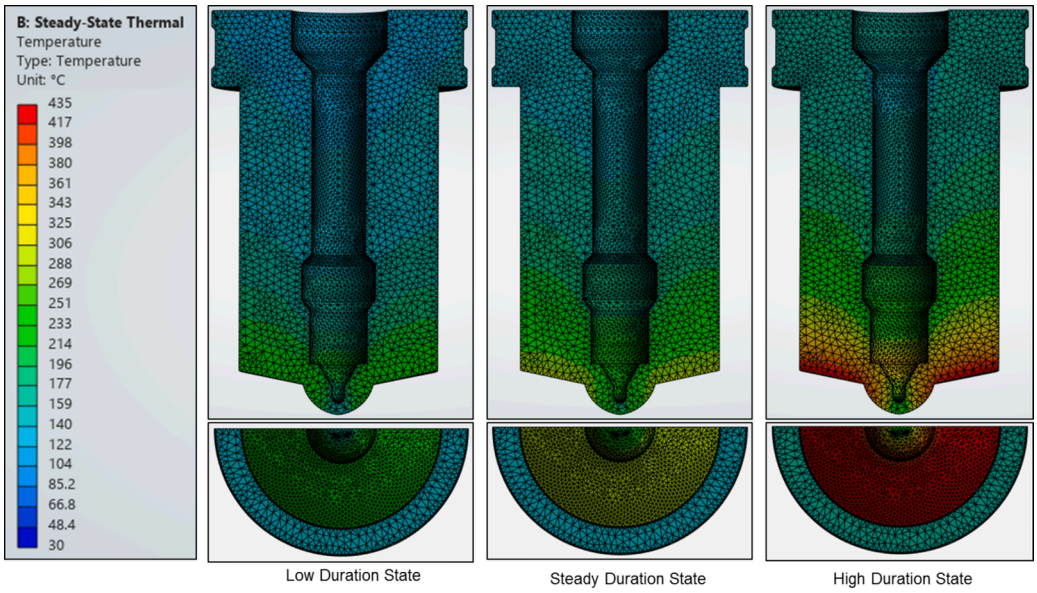

Fig. 16. Temperature distribution of injector seat.

temperatures, particularly above the material's temperature tolerance, cause irreversible damage to the insulation layer. This degradation diminishes the insulation's functional integrity, ultimately leading to a decline in overall solenoid coil performance and coil failure.

Injector malfunctions can lead to a reduction in fuel injection quantity, deterioration of atomisation quality and other related issues affecting engine performance. The injector's fundamental role is delivering fuel into the combustion chamber at high pressure, thereby ensuring proper fuel–air mixture formation and combustion efficiency. A malfunctioning injector may fail to deliver the required fuel quantity or achieve adequate atomisation, causing incomplete combustion, reduced power output and possible engine misfire. Therefore, monitoring in-cylinder pressure variations serves as a diagnostic indicator for identifying injector-related anomalies

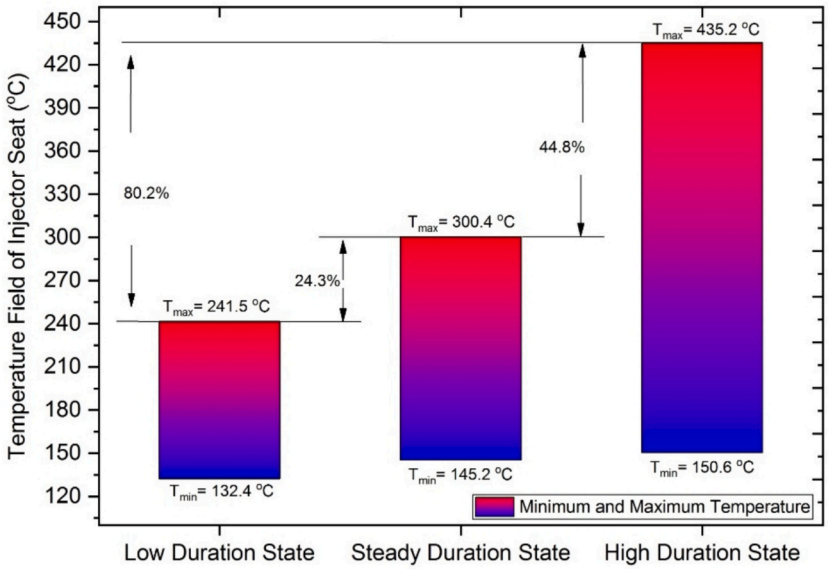

Fig. 17. Maximum and minimum temperature of injector seat in all states.

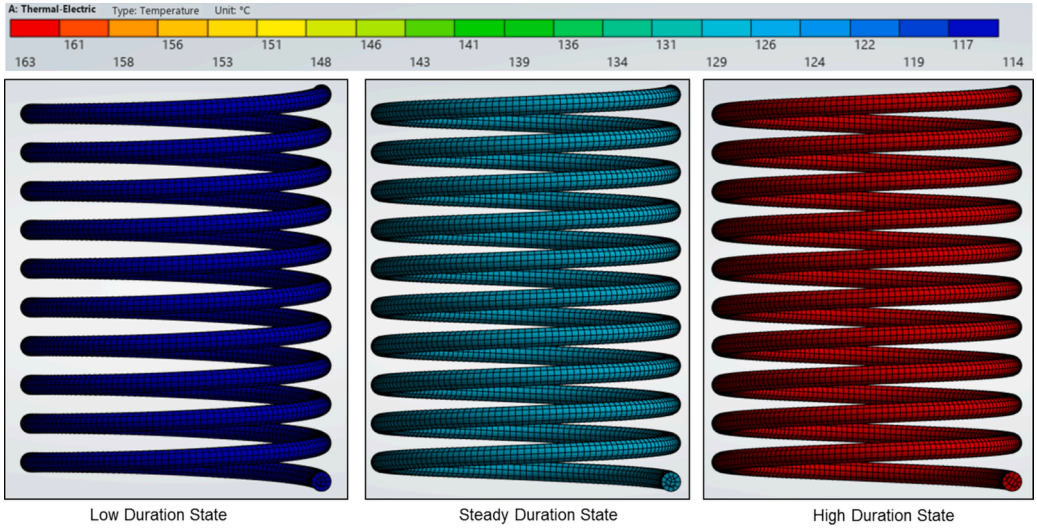

Fig. 18. Temperature field of coil.

Analysis of in-cylinder pressure signals enables detection of deviations from nominal pressure profiles, providing a robust diagnostic approach for injector fault identification and enhancing engine maintenance and performance evaluation assessment.

The in-cylinder temperature rises significantly under high load conditions, posing thermal stress that may compromise fuel injector performance and durability. Mitigating the adverse thermal effects on the injector requires effective in-cylinder temperature control strategies. One approach is to retard injection timing, which delays the combustion phase and moderates the rate of temperature rise within the cylinder. Another effective method is to adjust the air–fuel ratio. Using leaner mixtures by reducing fuel quantity or increasing air intake typically results in lower peak combustion temperatures. Additionally, increasing intake pressure enhances air density, leading to more complete combustion and contributing to lower in-cylinder temperatures. Collectively these measures contribute to better thermal management, thereby extending injector lifespan and maintaining optimal performance.

4. Conclusions

This study investigates the underlying causes of injector failure, through a combined approach involving both simulations and experimental methods. The abnormal operating behaviour of the injector is assessed using results obtained from Simulink-based simulations and experimental measurements. Then, a 3D thermal model is used to investigate the effects of in-cylinder temperature

on injector performance. The investigatioń s key findings are summarised as follows:

1. The idle control mode imposes a fuel demand limit of 4000 pptt during engine testing. When the load reaches approximately 267 kW, the speed controller fails to compensate for the additional fuel demand, leading to loss of control over the engine speed. At low engine-speeds (around 100 rpm), a sudden increase in the second injection duration, caused by the idle mode fuel demand limit, leads to transition-induced thermal stress and contributes to injector failure.
2. Velocity distribution within the injector remains relatively uniform across all operating states, except in the nozzle region. The fuel velocity reaches a maximum of approximately 47 m/s outside the nozzle area. However, the velocity increases sharply reaching to 620 m/s within the nozzle, indicating a steep velocity gradient. The highest velocities are located slightly below the centre of the nozzle, as shown by the red regions of the velocity contour map. The fuel velocity decreases near the nozzle walls due to the viscosity and velocity gradient effects. The thermal analysis demonstrates that the internal fuel temperature is predominantly governed by conjugate heat transfer from the heated injector structure. As the flow progresses toward the nozzle tip, combustion-chamber-induced heating increases the wall temperature, resulting in a gradual rise in fuel temperature and peak values near the injector seat region.
3. Injector heat transfer is governed by multiple boundary conditions, including fuel flow dynamics, in-cylinder gas convection and conduction from the cylinder head. The resulting temperature field is markedly non-uniform, typically increasing from the top toward the bottom of the injector. Both the temperature and the temperature gradient is highest at the bottom of the injector because here it is in direct contact with high-temperature combustion gases. In other regions of the injector, the inner surface maintains a lower temperature than the outer surface. This is attributed to the cooling effect of the fuel, which has a significantly lower temperature than the surrounding cylinder head material. A rapid increase in the fuel injection rate causes a sudden rise of the mixed gas temperature inside the cylinder, changing the thermal boundary conditions at the bottom of the injector. This change propagates through the injector body, affecting the overall temperature field and resulting in a noticeable change in the coil's ambient temperature. This studýs simulation results indicate that a 194 °C increase at the injector tip results in an equivalent rise in the maximum injector body temperature.
4. This rise in ambient temperature is the primary factor contributing to the increase in coil temperature. The instantaneous temperature changes within the cylinder led to variations in the coil's ambient temperature, which reached a maximum of around 163 ℃ in the high duration state. Thus, the combined influence of electrical current and elevated ambient temperature triggers the coiĺs thermal degradation. Prolonged exposure to temperatures exceeding its threshold causes the coil insulation material to lose its dielectric strength, leading to breakdown and eventual failure of the insulation. This degradation not only compromises the electrical insulation but also accelerates wear on the coil, leading to short circuits and coil failure.

CRediT authorship contribution statement

Seyfi Polat: Writing – original draft, Visualization, Software, Methodology, Investigation. **Xiaoguo Storm:** Writing – review & editing, Methodology, Investigation. **Martin Axelsson:** Writing – review & editing, Methodology, Investigation. **Jari Hyvönen:** Writing – review & editing, Methodology, Investigation. **Maciej Mikulski:** Writing – review & editing, Supervision, Project administration, Methodology, Funding acquisition, Conceptualization.

Declaration of competing interest

The authors declare the following financial interests/personal relationships which may be considered as potential competing interests: Maciej Mikulski reports financial support was provided by Bussines Finland. Xiaoguo Storm reports financial support was provided by Bussines Finland. Seyfi Polat reports financial support was provided by Bussines Finland. Seyfi Polat reports financial support was provided by TUBITAK. If there are other authors, they declare that they have no known competing financial interests or personal relationships that could have appeared to influence the work reported in this paper.

Acknowledgements

The work was conducted in the framework of the Flexible Clean Propulsion Technologies project with financial support from Business Finland (ref. 1310/31/2023). Additionally, the authors gratefully acknowledge the support of TÜBİTAK for providing a research scholarship to Seyfi Polat. The authors also thank Tan Qiushi for the valuable support provided during the initial stage of the manuscript preparation.

Data availability

No data was used for the research described in the article.

References

[1] J. Liu, Y. Liu, Q. Ji, P. Sun, X. Zhang, X. Wang, H. Ma, Effects of split injection strategy on combustion stability and GHG emissions characteristics of natural gas/diesel RCCI engine under high load, Energy 266 (2023) 126542, https://doi.org/10.1016/j.energy.2022.126542.

[2] A. Kakoee, Y. Bakhshan, A. Barbier, P. Bares, C. Guardiola, Modeling combustion timing in an RCCI engine by means of a control oriented model, Control Eng. Pract. 97 (2020) 104321, https://doi.org/10.1016/j.conengprac.2020.104321.
[3] K.Q. Bui, L.P. Perera, J. Emblemsvåg, Life-cycle cost analysis of an innovative marine dual-fuel engine under uncertainties, J. Clean. Prod. 380 (2022) 134847, https://doi.org/10.1016/j.jclepro.2022.134847.
[4] Y. Ke, C. Yao, E. Song, Q. Dong, L. Yang, An early fault diagnosis method of common-rail injector based on improved CYCBD and hierarchical fluctuation dispersion entropy, Digital Signal Process. 114 (2021) 103049, https://doi.org/10.1016/j.dsp.2021.103049.
[5] M. Gallego, J. San Román, G.L. Bianchi, J.L. Otegui, Influence of fluid flow in microbiological corrosion failures in oil field injector well tubing, Eng. Fail. Anal. 128 (2021) 105603, https://doi.org/10.1016/j.engfailanal.2021.105603.
[6] A. Taghizadeh-Alisaraei, A. Mahdavian, Fault detection of injectors in diesel engines using vibration time-frequency analysis, Appl. Acoust. 143 (2019) 48–58, https://doi.org/10.1016/j.apacoust.2018.09.002.
[7] E. Song, Y. Ke, C. Yao, Q. Dong, L. Yang, Fault diagnosis method for high-pressure common rail injector based on IFOA-VMD and hierarchical dispersion entropy, Entropy 21 (10) (2019) 923, https://doi.org/10.3390/e21100923.
[8] J. Monieta, Diagnosing cracks in the injector nozzles of marine internal combustion engines during operation using vibration symptoms, Appl. Sci. 13 (17) (2023) 9599, https://doi.org/10.3390/app13179599.
[9] W.Q. Li, Z.R. Xue, H.B. Ke, H. Wan, X.G. Wei, F. Qin, G.Q. He, Thermal analysis of a high-efficiency internally-cooled strut injector for scramjet engine, Int. J. Therm. Sci. 163 (2021) 106811, https://doi.org/10.1016/j.ijthermalsci.2020.106811.
[10] A. Chakravarty, N. Biswas, K. Ghosh, Impact of side injection on heat removal from truncated conical heat-generating porous bed: thermal non-equilibrium approach, J. Therm. Anal. Calorim. 143 (2021) 3741–3760, https://doi.org/10.1007/s10973-020-09295-6.
[11] Y. Liu, J. Liu, C. Tang, H. Wang, Thermal analysis of magnetron injection gun for 170 GHz gyrotron, Microw. Opt. Technol. Lett. 62 (1) (2020) 72–75, https://doi.org/10.1002/mop.32397.
[12] X. Xu, Z. Yu, Y. Gao, Micro-cracks on electro-discharge machined surface and the fatigue failure of a diesel engine injector, Eng. Fail. Anal. 32 (2013) 124–133, https://doi.org/10.1016/j.engfailanal.2013.03.011.
[13] X. Xu, Z. Yu, Failure analysis of a truck diesel engine injector nozzle-valve, Eng. Fail. Anal. 120 (2021) 105084, https://doi.org/10.1016/j.engfailanal.2020.105084.
[14] O. Asi, Failure of a diesel engine injector nozzle by cavitation damage, Eng. Fail. Anal. 13 (7) (2006) 1126–1133, https://doi.org/10.1016/j.engfailanal.2005.07.021.
[15] Wärtsilä Finland Oy. (2017). Wärtsilä 20 Instruction Manual.
[16] Y. Hu, J. Yang, N. Hu, Experimental study and optimization in the layouts and the structure of the high-pressure common-rail fuel injection system for a marine diesel engine, Int. J. Engine Res. 22 (6) (2020) 1865–1878, https://doi.org/10.1177/1468087420921610.
[17] W. Niklawy, M. Shahin, M.I. Amin, A. Elmaihy, Modelling and experimental investigation of high-pressure common rail diesel injection system, IOP Conf. Ser.: Mater. Sci. Eng. 973 (1) (2020) 012037, https://doi.org/10.1088/1757-899X/973/1/012037.
[18] Y. Bai, Q. Lan, L. Fan, X. Ma, H. Liu, Investigation on the fuel injection stability of high-pressure common rail system for diesel engines, Int. J. Engine Res. 22 (2) (2019) 617–632, https://doi.org/10.1177/1468087419856989.
[19] Tran, T. A. (2020). Analysis of the PID controller for marine diesel engine speed on Simulink environment. In 2020 International Conference on Electrical Engineering and Control Technologies (CEECT) (pp. 1–5). IEEE. Doi: 10.1109/CEECT50755.2020.9298679.
[20] F.R. Menter, R.B. Langtry, S.R. Likki, Y.B. Suzen, P.G. Huang, S. Völker, A correlation-based transition model using local variables—Part I: model formulation, J. Turbomach. 128 (3) (2006) 413–422, https://doi.org/10.1115/1.2184352.
[21] T. Qiu, X. Song, Y. Lei, X. Liu, X. An, M. Lai, Influence of inlet pressure on cavitation flow in diesel nozzle, Appl. Therm. Eng. 109 (2016) 364–372, https://doi.org/10.1016/j.applthermaleng.2016.08.060.
[22] C.H. Achebe, B.M.O. Ogunedo, J.L. Chukwuneke, N.B. Anosike, Analysis of diesel engine injector nozzle spray characteristics fueled with residual fuel oil, Heliyon 6 (8) (2020) e04637, https://doi.org/10.1016/j.heliyon.2020.e04637.
[23] W. Zuo, Q. Li, Z. He, Y. Li, Numerical investigations on thermal performance enhancement of hydrogen-fueled micro planar combustors with injectors for micro-thermophotovoltaic applications, Energy 194 (2020) 116904, https://doi.org/10.1016/j.energy.2020.11690.
[24] L. Fonseca, P. Olmeda, R. Novella, Internal combustion engine heat transfer and wall temperature modeling: an overview, Arch. Comput. Meth. Eng. 27 (2020) 1661–1679, https://doi.org/10.1007/s11831-019-09361-9.
[25] C. Dere, C. Deniz, Effect analysis on energy efficiency enhancement of controlled cylinder liner temperatures in marine diesel engines with model-based approach, Energ. Conver. Manage. 220 (2020) 113015, https://doi.org/10.1016/j.enconman.2020.113015.